The University of Southern Mississippi

The Aquila Digital Community

9-1-2015

Indirect Evidence For Substantial Damping of Low-Mode Internal Tides In the Open Ocean

Joseph K. Ansong
University of Michigan, Ann Arbor, jkansong@umich.edu

Brian K. Arbic
University of Michigan, Ann Arbor

Maarten C. Buijsman
University of Southern Mississippi, maarten.buijsman@usm.edu

James G. Richman
Naval Research Laboratory

Jay F. Shriver
Naval Research Laboratory

See next page for additional authors

Follow this and additional works at: https://aquila.usm.edu/fac_pubs

Part of the Oceanography and Atmospheric Sciences and Meteorology Commons

Authors

Joseph K. Ansong, Brian K. Arbic, Maarten C. Buijsman, James G. Richman, Jay F. Shriver, and Alan J. Wallcraft

JGR

RESEARCH ARTICLE

Correspondence to:
J. K. Ansong,
jkansong@umich.edu

Indirect evidence for substantial damping of low-mode internal tides in the open ocean

Joseph K. Ansong[1], Brian K. Arbic[1], Maarten C. Buijsman[2], James G. Richman[3], Jay F. Shriver[3], and Alan J. Wallcraft[3]

[1]Department of Earth & Environmental Sciences, University of Michigan, Ann Arbor, Michigan, USA, [2]Department of Marine Science, University of Southern Mississippi, Stennis Space Center, Mississippi, USA, [3]Ocean Dynamics and Prediction Branch, Code 7323, Naval Research Laboratory, Stennis Space Center, Mississippi, USA

Abstract A global high-resolution ocean circulation model forced by atmospheric fields and the M_2 tidal constituent is used to explore plausible scenarios for the damping of low-mode internal tides. The plausibility of different damping scenarios is tested by comparing the modeled barotropic tides with TPXO8, a highly accurate satellite-altimetry-constrained tide model, and by comparing the modeled coherent baroclinic tide amplitudes against along-track altimetry. Five scenarios are tested: (1) a topographic internal wave drag, argued here to represent the breaking of unresolved high vertical modes, applied to the bottom flow (default configuration), (2) a wave drag applied to the barotropic flow, (3) absence of wave drag, (4) a substantial increase in quadratic bottom friction along the continental shelves (with wave drag turned off), and (5) application of wave drag to the barotropic flow at the same time that quadratic bottom friction is substantially increased along the shelves. Of the scenarios tested here, the default configuration (1) yields the most accurate tides. In all other scenarios (2–5), the lack of damping on open ocean baroclinic motions yields baroclinic tides that are too energetic and travel too far from their sources, despite the presence of a vigorous mesoscale eddy field which can scatter and decohere internal tides in the model. The barotropic tides are also less accurate in the absence of an open ocean damping on barotropic motions, that is, in scenarios (3) and (4). The results presented here suggest that low-mode internal tides experience substantial damping in the open ocean.

1. Introduction

A long-standing problem in physical oceanography is the determination of locations where tides, including low-mode internal tides, dissipate their energy. An answer to this problem will help constrain the spatial variability in ocean mixing patterns and consequently lead to more physically based mixing parameterizations for global ocean circulation models. It has been argued that mixing driven by breaking internal tides and other internal waves exerts a strong influence on the stratification and general circulation of the ocean, with consequent implications for climate variability [*Munk*, 1966; *Munk and Wunsch*, 1998; *Wunsch and Ferrari*, 2004].

Using barotropic tidal models constrained by TOPEX/Poseidon satellite altimeter data, *Egbert and Ray* [2000, 2001] clearly demonstrated that a significant percentage (25–30%) of barotropic tidal energy is lost in open ocean regions of rough topography. The energy loss in the Egbert and Ray studies represents the net effect of mechanisms that siphon energy from the barotropic tide including conversion to baroclinic tides as well as loss to quadratic bottom boundary layer drag (hereafter referred to as "quadratic bottom friction"). Because internal tides were not directly simulated in the Egbert and Ray studies, they could not discriminate between barotropic tidal energy loss due to local dissipation and due to generation and radiation of internal tides. Using along-track data from the TOPEX/Poseidon satellite-altimetry mission, *Ray and Mitchum* [1996, 1997] revealed the surface manifestations of the coherent low-mode internal tides that propagate up to 1000 km from sources such as the Hawai'ian Ridge [also see *Alford and Zhao*, 2007; *Zhao et al.*, 2010]. The long-range propagation of internal tides from sources such as Hawai'i has also been revealed in an analysis of acoustic tomography [*Dushaw et al.*, 1995] and an analysis of tide gauge data supplemented with inverted echo sounders [*Mitchum and Chiswell*, 2000]. Where and how these low-mode internal tides are damped is a topic of great interest in the community.

Direct simulation of baroclinic tides has been done on regional scales [e.g., *Carter et al.*, 2012, and references therein] and basin scales [e.g., *Niwa and Hibiya*, 2001], as well as, more recently, global scales. Using three-dimensional ocean models forced by only the astronomical tidal potential, *Arbic et al.* [2004] and *Simmons et al.* [2004] directly simulated the global baroclinic tides, further revealing the rich structure of the internal tide climate in the ocean. *Arbic et al.* [2010] later showed that this rich structure can still be captured in a model that is simultaneously forced by both the astronomical tidal potential and atmospheric fields [see also *Arbic et al.*, 2012; *Müller et al.*, 2012; *Waterhouse et al.*, 2014] (C. B. Rocha, Mesoscale to submesoscale wavenumber spectra in Drake Passage, submitted to *Journal of Physical Oceanography*, 2015, based on simulations by D. Menemenlis (personal communication, 2014, 2015)). Because high-resolution global models with simultaneous atmospheric and tidal forcing are expensive and relatively new, no comprehensive investigation has been done thus far of internal tide damping in such models.

Several mechanisms have been identified in the literature as potential dissipators of the internal tides. After generation, the high-vertical-mode internal tides may break locally [*Klymak et al.*, 2006, 2008; *Legg and Klymak*, 2008; *Buijsman et al.*, 2012] while the remaining low-mode tides propagate away from their topographic sources. Propagating low-mode tides may dissipate via interactions with distant topographies [*Johnston and Merrifield*, 2003; *Mathur et al.*, 2014] or through interactions with mean flows and eddies [*St. Laurent and Garrett*, 2002; *Rainville and Pinkel*, 2006; *Dunphy and Lamb*, 2014; *Kerry et al.*, 2014]. They may also lose energy through upper-ocean wave-wave interactions, for instance through the parametric subharmonic instability (PSI) mechanism [*McComas and Bretherton*, 1977; *Müller et al.*, 1986; *Staquet and Sommeria*, 2002; *MacKinnon and Winters*, 2005; *Simmons*, 2008; *Sun and Pinkel*, 2012, 2013]. Finally, low-mode internal tides may propagate onto continental shelves and subsequently dissipate, thus mixing the coastal ocean [*Nash et al.*, 2004; *Martini et al.*, 2011; *Kelly et al.*, 2013; *Waterhouse et al.*, 2014]. Detailed discussions of the above mechanisms can be found in previous publications [e.g., *St. Laurent and Garrett*, 2002; *Kunze and Llewellyn Smith*, 2004]. The relative importance of each of these mechanisms in the global ocean is unclear at present.

Global ocean models have become indispensable in understanding large-scale oceanic motions, due to their widespread spatial coverage, relatively frequent output and relatively low cost compared with observational systems. Nevertheless, global models have many shortcomings. For instance, global models are not able to resolve the breaking of internal gravity waves. Justifications for the usage of a parameterized wave drag in global barotropic tide models are expounded upon in several studies [e.g., *Jayne and St. Laurent*, 2001; *Arbic et al.*, 2004; *Egbert et al.*, 2004; *Green and Nycander*, 2013; *Buijsman et al.*, 2015]. Among others, *Arbic et al.* [2004, 2010] argued that the generation of low-mode internal tides in current state-of-the-art global internal tide models does not preclude the need for an explicit damping of low-mode internal tides in such models, which are unable to resolve generation and breaking of high-mode internal waves. In *Arbic et al.* [2004, 2010] and in subsequent related papers [e.g., *Shriver et al.*, 2012; *Buijsman et al.*, 2015], it was argued that a parameterized wave drag acting on the bottom flow can be taken to represent the generation and breaking of unresolved high modes by flow over rough topography. Simultaneously *Shriver et al.* [2012] showed that the barotropic and low-mode baroclinic tides from simulations forced by tides and atmospheric fields compare well to satellite altimeter observations when a parameterized internal wave drag is applied to the bottom flow. Note that because the bottom flow has both barotropic and low-mode baroclinic components, such a drag damps low-mode internal tides as well as barotropic tides.

We can test some of the aforementioned low-mode internal tide damping mechanisms, by applying them to global internal tide simulations and comparing the resulting barotropic and baroclinic tides with altimetry-constrained models and observations, as was done in *Shriver et al.* [2012] for a wave drag acting on the bottom flow. By comparing the resulting tides to observations, we can determine which drag mechanisms are plausible and which are not. In the scenarios we are testing, we will

a. apply parameterized topographic internal wave drag on the bottom flow (referred to as the "default configuration" or "bottom wave drag"),
b. apply wave drag on only the barotropic tides (referred to as "barotropic wave drag"),
c. remove the wave drag entirely,
d. remove wave drag and substantially increase quadratic bottom friction along the shelves, and
e. apply wave drag on only the barotropic tides and at the same time substantially increase quadratic bottom friction along the shelves.

Scenario (a) represents scattering into high modes above rough topography. We note that we will vary the strength of the wave drag in scenario (a) but will refer to all such simulations with wave drag applied on the bottom flow as "default configuration" or "bottom wave drag." In scenario (b), only the barotropic mode experiences topographic scattering, and again we will vary the drag strength in this scenario. In scenario (c), neither barotropic nor low-mode baroclinic tides experience substantial damping in the open ocean. Scenario (d) represents the hypothesis that most damping of low-mode tides occurs in shallow waters. Scenario (e) is a combination of (b) and (d) that prevents overly energetic generation of baroclinic tides in the open ocean while still testing whether most damping of low-mode internal tides occurs along the shelves. The scenarios (a)–(e) are not an exhaustive list of potential low-mode internal tide damping mechanisms. Damping by upper-ocean wave-wave interactions is not tested here and will instead be tested in a paper under preparation, in which simplified global tidal models (with only tidal forcing) will be used. Furthermore, damping of low-mode tides in the actual ocean is likely to arise from more than one mechanism. However, it is too complicated and expensive in this first study to utilize complex combinations of different mechanisms in our simulations. Our simulations represent various limiting cases and will likely point further studies in fruitful directions. We further note that because energy budget analyses of our simulations are complex and computationally expensive, we do not undertake them here and instead will report on them elsewhere. A detailed energy budget analysis for one of our previous HYCOM simulations is in review (M. C. Buijsman et al., Impact of internal wave drag on the semidiurnal energy balance in a global ocean circulation model, submitted to *Journal of Physical Oceanography*, 2015). Our focus in the present paper is on testing the plausibility of extreme damping scenarios.

It should be noted that in all scenarios examined in this paper, the presence of atmospheric forcing in a high-resolution model ensures a vigorous mesoscale eddy field [*Hecht and Hasumi*, 2008; *Thoppil et al.*, 2011]. The mesoscale eddies will decrease the coherence of the internal tides, or in other words, will render a nonstationary component of the internal tide field [e.g., *Shriver et al.*, 2014]. Because along-track altimetry only detects the coherent component of baroclinic tides, it has been argued that the general weakness of low-mode tides far from their sources seen in global maps made from altimetry could reflect tidal incoherence arising from scattering by eddies, rather than damping. Because eddy scattering is present in our simulations, the presence of baroclinic tides in our model that are stronger than or propagate farther than tides in observations will be taken as evidence of under-damping in the model, rather than a signature of an under-represented scattering, as could be the case in a tide-only model.

To our knowledge, global baroclinic tide simulations representing cases (b), (d), and (e) have not been reported before. Several results [*Arbic et al.*, 2010, 2012; *Richman et al.*, 2012; *Shriver et al.*, 2012, 2014; *Timko et al.*, 2012, 2013; *Müller et al.*, 2015] have been published on case (a) using simulations of the Hybrid Coordinate Ocean Model (HYCOM) [*Bleck*, 2002; *Chassignet et al.*, 2003; *Halliwell*, 2004]. The *Arbic et al.* [2010] simulation was preliminary and has not been used in any of our subsequent papers. The case (a) scenario used in the other HYCOM papers mentioned above was run for a long time and will prove useful in this paper, which focuses most of its attention on runs performed for the first time here. Global baroclinic tide simulations in some previous studies [*Simmons et al.*, 2004; *Simmons*, 2008; *Müller et al.*, 2012; *Waterhouse et al.*, 2014] were performed without utilizing a parameterized topographic wave drag (referred to as case c above). To obtain accurate barotropic tides in their basin and global models, *Niwa and Hibiya* [2001, 2011] employed a linear damping scheme, representing energy loss via nonlinear interactions with the background internal waves and mesoscale eddies, to account for the decay of internal tides as they propagate from their sources.

In the next section, we present the HYCOM simulations utilized in this paper and the diagnostics we will employ to compare the model output with observations. Section 3 presents the results of the simulated barotropic and baroclinic tides and their comparison with observations under the different drag scenarios. Section 4 presents the summary and conclusions.

2. Model and Diagnostics

2.1. The Model

This study utilizes simulations of HYCOM, which is used by the United States Navy as an operational model. The HYCOM simulations presented here are run in forward (non-data-assimilative) mode and utilize 41

Table 1. Description of the Different Simulations and the Strength of the Applied Wave Drag and Quadratic Bottom Friction[a]

Simulation	Description	Drag Scale Factor
E053	No-wave drag	0.0
E054	Increased bottom friction (×25) along shelves	0.0
E055	Increased bottom friction (×100) along shelves	0.0
E072	Wave drag on bottom flow	0.2
E073	Wave drag on barotropic flow	0.2
E051	Wave drag on bottom flow	0.5
E052	Wave drag on barotropic flow	0.5
E074	Wave drag on barotropic flow and increased bottom friction (×100) along shelves	0.5
E056	Wave drag on bottom flow	0.7
E057	Wave drag on barotropic flow	0.7
E058	Wave drag on bottom flow	1.0
E059	Wave drag on barotropic flow	1.0

[a]In E054, E055, and E074, the bottom friction (C_d) along the shelves (depths <2500 m) is increased by about 25 and 100 times, respectively, above the value in the deep ocean ($C_d = 0.0025$) (see text for additional explanation).

hybrid vertical layers on a global tri-pole grid with a nominal horizontal resolution, at the equator, of 1/12.5°. The simulations are forced by the M_2 tide, the largest tidal constituent in the ocean, and by hourly atmospheric fields from the Navy Global Environmental Model (NAVGEM) [*Hogan et al.*, 2014]. The initial state is from a case with HYCOM coupled to the Los Alamos sea ice model (CICE) [*Hunke and Lipscomb*, 2008], initialized from a January climatology, spun up with climatological atmospheric forcing for 7 model years and then run from 2003 to June 2011 using Navy Operational Global Atmospheric Prediction Sys-

tem (NOGAPS) [*Rosmond et al.*, 2002] atmospheric forcing. NAVGEM replaced NOGAPS as the US Navy's operational global numerical weather prediction system in 2013. Our simulations began to use NAVGEM in June 2011 because we have hourly NAVGEM fields for that time period. The June 2011 ocean from HYCOM was first extended under the Antarctic ice shelf, to improve tidal accuracy, and CICE was replaced by HYCOM's built-in thermodynamic sea ice model to save computer time. HYCOM has several options for tidal Self Attraction and Loading (SAL) [*Hendershott*, 1972]. Here we use the observed SAL, calculated from the data-assimilative TPXO8-atlas [*Egbert and Erofeeva*, 2002, updated], for all cases. Most of the simulations here are run from July 2011 to March 2012. Hourly sea surface height (SSH) data were saved for the last 3 months (January–March 2012) of each simulation. Four simulations were run for a longer period of 10 months to investigate the dependence of the results upon the length of time series as will be discussed in section 3.2.2.

In this paper, we employ the topographic wave drag scheme by *Jayne and St. Laurent* [2001]. The drag was tuned in baroclinic HYCOM simulations with different scale factors showing that a scale factor of 0.5 is optimum. Other scale factors will also be utilized in our simulations. Our previous HYCOM simulations [e.g., *Shriver et al.*, 2012] used the scheme by *Garner* [2005]. Here we turn to the *Jayne and St. Laurent* [2001] scheme because of its simplicity and smoother nature [*Green and Nycander*, 2013; *Buijsman et al.*, 2015] which makes it easier to use in baroclinic models and less prone to numerical instabilities. We performed two additional simulations with the Garner scheme showing that it also gives good barotropic and baroclinic tides. Later, we will also turn to an older simulation (designated internally as HYCOM 18.5) that employed the *Garner* [2005] drag scheme, and that has been used in many of our HYCOM tides papers to date [e.g., *Shriver et al.*, 2012, among others]. The older simulation was run out for 5 years and will be useful for our analysis of the impact of record durations at the end of the results section. A brief discussion of the wave drag schemes by *Jayne and St. Laurent* [2001] and *Garner* [2005] is given below. Thorough discussions on topographic wave drag and quadratic bottom friction and their appearance in the momentum equations can be found in previous publications [e.g., *Arbic et al.*, 2004, 2010; *Buijsman et al.*, 2015]. In particular, *Arbic et al.* [2010] discuss the subtleties involved in applying wave drag to only the tidal flow in HYCOM simulations that simultaneously resolve both tidal and nontidal motions. Table 1 displays the 12 different simulations conducted for this paper with additional details to be explained below.

2.2. Topographic Wave Drag Schemes

The topographic wave drag scheme by *Jayne and St. Laurent* [2001] is represented by a linear drag coefficient that varies spatially based upon the topography [also see *Green and Nycander*, 2013; *Buijsman et al.*, 2015], viz:

$$C_{JSL} = \alpha \frac{\pi}{L} \hat{H}^2 N_b, \tag{1}$$

where $\hat{H}$ is the bottom roughness, N_b is the buoyancy frequency at the bottom, and L is the wave length of the topography. L is set to 10 km and $\alpha = 1$ in *Jayne and St. Laurent* [2001]. This bottom wave drag
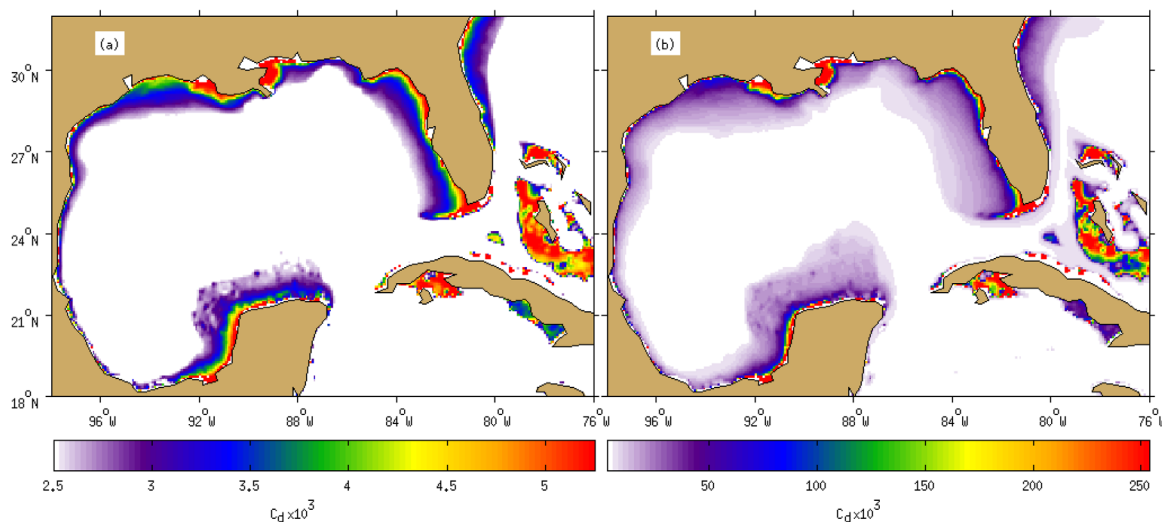
Figure 1. Map of variable bottom friction around the Gulf of Mexico, using (a) the nominal choice of $z_0 = 10$ mm and (b) $z_0 = 1.13$ m (resulting in quadratic drag coefficient that can be about 100 times larger than the deep ocean value of 0.0025). Note the different scales used in the two subplots.

coefficient acts upon flow in the bottom 500 m, which is taken as a typical vertical scale length for internal tides following discussions in *St. Laurent and Garrett* [2002]. In HYCOM, α is used as a wave drag scale factor (or a tuning parameter) to tune the model for accurate barotropic and baroclinic tides with respect to observations. Different values of α are utilized in the simulations presented in this paper.

The scheme by *Garner* [2005] is based on an exact analytical solution for drag in the limit of arbitrary small-amplitude topography. The scheme is supplemented by scaling arguments to account for nonlinear blocking effects. As with the *Jayne and St. Laurent* [2001] scheme, the *Garner* [2005] scheme takes the buoyancy frequency at the bottom, and the seafloor topographic field, as inputs. For simplicity, the original tensor scheme in *Garner* [2005] is reduced to a scalar form in our HYCOM simulations. As with the *Jayne and St. Laurent* [2001] scheme, the *Garner* [2005] scheme is applied over the bottom 500 m of the flow. *Arbic et al.* [2010] provide more details of the *Garner* [2005] scheme and its implementation in HYCOM.

The strength of the wave drag can be measured by computing the spatially averaged decay rate. In the case of the scheme by *Jayne and St. Laurent* [2001], this is given by [*Arbic et al.*, 2004]

$$r_{average} = \frac{\int \int (C_{JSL}/H)\mathrm{d}A}{\int \int \mathrm{d}A}, \qquad (2)$$

where H is the resting water depth and $\mathrm{d}A$ is an element of area. We computed the spatially averaged decay rate in waters deeper than 1000 m for wave drag scale factors of 0.5 and 1.0 and obtained $(3.8\,\text{days})^{-1}$ and $(1.9\,\text{days})^{-1}$, respectively. A similar calculation for our older simulation using the *Garner* [2005] scheme with a drag scale factor of 12 gives $(1.3\,\text{days})^{-1}$. We note that these numbers are comparable to the $(\sim 2.0\,\text{days})^{-1}$ decay rate computed by *Arbic et al.* [2004] for their barotropic tide simulations.

2.3. Bottom Friction Along the Shelves

In the typical HYCOM configuration [see *Buijsman et al.*, 2015], the quadratic drag coefficient is 0.0025 in deep water and is a function of depth [*Schlichting*, 1968; *Oey*, 2006]

$$C_d = \left[\frac{\kappa}{\log(0.5H/z_0)} \right]^2 \qquad (3)$$

in shallow water, where $\kappa = 0.4$ is the von Karman constant, z_0 is the roughness parameter, and H is the resting water depth. The nominal choice of $z_0 = 10$ mm gives values of C_d that are about twice as high as 0.0025 for depths shallower than about 60 m.

To substantially increase the bottom friction along the shelves for cases (d) and (e) described earlier, we restrict $C_d=0.0025$ for all locations having seafloor depths greater than 2500 m. We then choose two different values of z_0 (0.5 and 1.13 m) to determine the values of C_d along the shelves using equation (3). The first choice $z_0=0.5$ m results in C_d that can be about 25 times higher than 0.0025 around the shelves (see Figure 1 for an example plot around the Gulf of Mexico) while the second choice results in C_d that can be about 100 times above 0.0025. The first choice is utilized in simulation E054 of Table 1, while the second choice is utilized in simulations E055 and E074.

2.4. Diagnostics

We evaluate the accuracy of tides in the different simulations by computing the signal size (S) and the root-mean-square error (RMSE) from time series of SSH. The barotropic tides are validated against the TPXO8-atlas sea surface elevations while the baroclinic tides are compared to almost 17 years of along-track TOPEX/Poseidon and Jason satellite altimeter data [*Ray and Mitchum*, 1996; *Ray and Byrne*, 2010; *Shriver et al.*, 2012; R. Ray, personal communication, 2011]. Details of the analysis approach used to extract baroclinic tides from the HYCOM output and along-track altimeter data are outlined in *Shriver et al.* [2012]. In brief, HYCOM output is interpolated to the altimeter tracks. For both HYCOM and altimeter output, spatial band-pass filtering along the altimeter tracks is used to extract the M_2 internal tide signals with wavelengths in the 50–400 km range. Only locations with sea floor depth greater than 1500 m are examined. The RMSE is defined as [*Arbic et al.*, 2004]

$$RMSE = \sqrt{\frac{\int\int RMSE_t^2 \, dA}{\int\int dA}} \qquad (4)$$

and

$$RMSE_t = \sqrt{\langle [\eta_m(t) - \eta_o(t)]^2 \rangle}, \qquad (5)$$

where η is sea surface elevation, subscripts "m" and "o" refer to model and observations, respectively, t is time, $<\,>$ represents time averaging, and dA is an element of area. By writing the modeled and observed elevations as $\eta_m(t) = A_m\cos(\omega t - \phi_m)$ and $\eta_o(t) = A_o\cos(\omega t - \phi_o)$, where A and ϕ are the amplitude and phase of the signals, respectively, $RMSE_t$ greatly simplifies to [e.g., *Cummins and Oey*, 1997]

$$RMSE_t = \sqrt{\frac{1}{2}(A_m - A_o)^2 + A_m A_o [1 - \cos(\phi_m - \phi_o)]}. \qquad (6)$$

The signal of the model elevations is defined as [*Arbic et al.*, 2004]

$$S = \sqrt{\frac{\int\int <[\eta_m(t)]^2> \, dA}{\int\int dA}} = \sqrt{\frac{\int\int \frac{1}{2}A_m^2 \, dA}{\int\int dA}}, \qquad (7)$$

while the signal of the observations is similar, with η_m and A_m replaced by η_o and A_o, respectively.

3. Results

3.1. Barotropic Tides

Amplitude and phase maps of the M_2 surface elevations in TPXO8 and HYCOM are shown in Figure 2. Surface elevations in HYCOM include the internal tide but are dominated by the barotropic tide. The HYCOM simulations displayed in Figures 2b–2d show qualitatively similar spatial distributions to those in TPXO8. They capture almost all amphidromic locations correctly except at the Antarctic coast around 160°W where Figures 2c and 2d deviate from TPXO8. A notable difference occurs around the Amazon and the east coast of America where HYCOM underpredicts tidal amplitudes. HYCOM simulations in which the wave drag is completely turned off (Figure 2e), and in which there is a strong increase of quadratic bottom friction along the shelves but with a turned-off wave drag (e.g., Figure 2f), produce barotropic tides that are overly energetic relative to
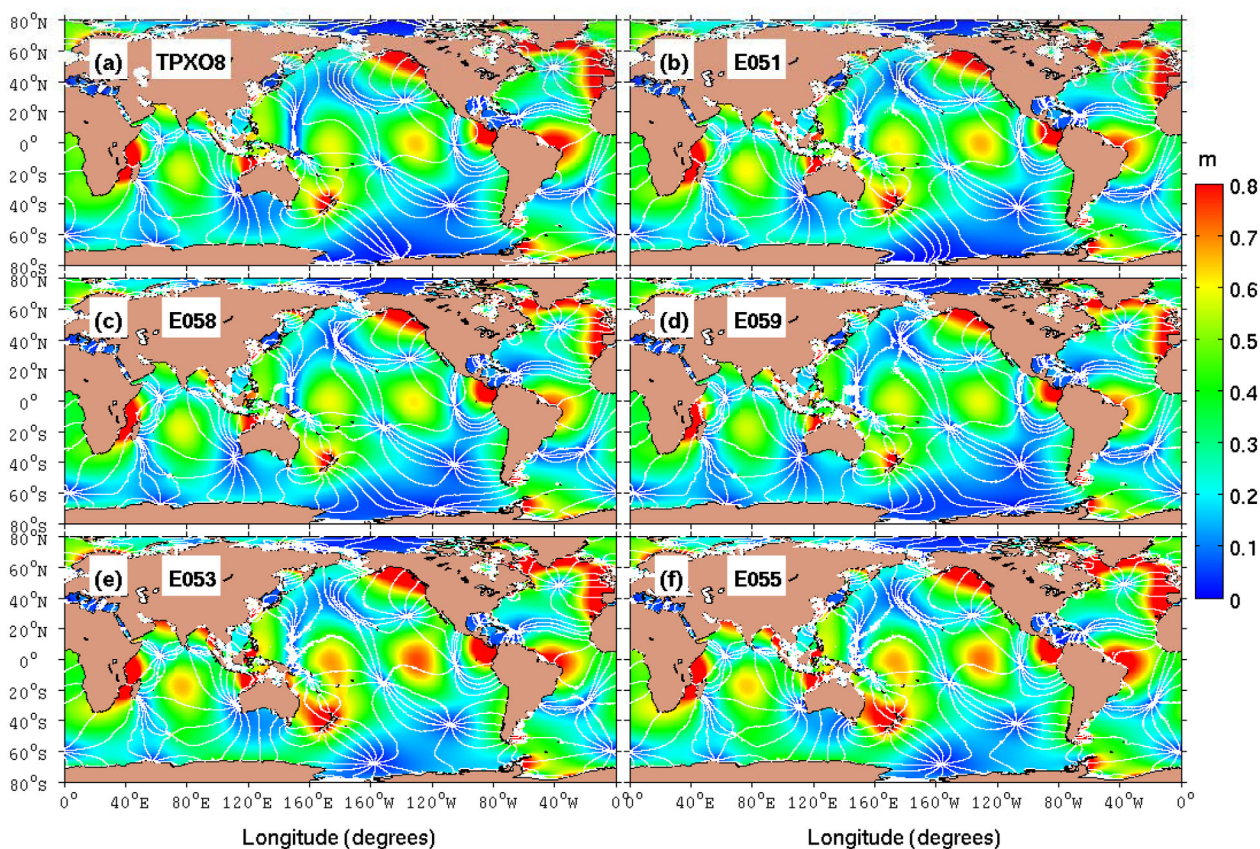
Figure 2. Amplitude (colors) and phase (white contours separated by 30°) of the M_2 surface elevation in (a) TPX08-atlas, a barotropic tide model constrained by satellite altimetry, and HYCOM simulations (b) E051; with wave drag (scale factor = 0.5) applied to the bottom flow, (c) E058; with wave drag (scale factor = 1.0) applied to the bottom flow, (d) E059; with wave drag (scale factor = 1.0) applied to only the barotropic flow, (e) E053; without wave drag, (f) E055; without wave drag but with quadratic bottom friction increased by about 100 times along the continental shelves.

TPXO8. This is especially visible in the Pacific and Indian oceans, although the amplitudes in the Amazon region appear more similar to observations than they do in the simulations with wave drag.

Figure 3 (black curves) displays the RMSE in the HYCOM simulations measured against TPXO8 showing that the bottom wave drag simulation E051 (with wave drag scale factor of 0.5) yields the most accurate barotropic tides. For any given scale factor of the wave drag, we see that more accurate barotropic tides are obtained if the wave drag is applied to the bottom flow (bottom wave drag; simulations E051, E056, E058, and E072). Application of the wave drag to only the barotropic component of the flow (barotropic wave drag; simulations E052, E057, E059, and E073) results in somewhat less accurate barotropic tides compared to their counterparts with the bottom wave drag. Completely removing the wave drag (simulation E053) increases the barotropic SSH error by about 2.0 cm above that of the most accurate bottom wave drag case (simulation E051). This is because the absence of a wave drag results in overly energetic barotropic tides as seen in Figure 2e. Figure 3 also shows that increasing the quadratic bottom friction along the shelves, without including a wave drag, yields the largest RMSE values (E054 and E055). Simulation E074 is similar to E052 (both have a barotropic wave drag) except that E074 has large quadratic bottom friction along the shelves. The additional increase in bottom friction in E074 yields slightly less accurate tides. Note that the plots of RMSE in Figure 3 display results for three different months of model output from each simulation. We find that there is very little monthly variance in the barotropic tidal RMSE. We performed a similar RMSE analysis on the barotropic tides using 3 month-long SSH data and found that the results were little different from the 1 month analysis results. This contrasts with our findings in the case of the internal tides, to be discussed later.

The magenta curves in Figure 3 display the signal S of each simulation and that of TPXO8. We find that the signal generally decreases with increasing scale factor, because more energy is removed from
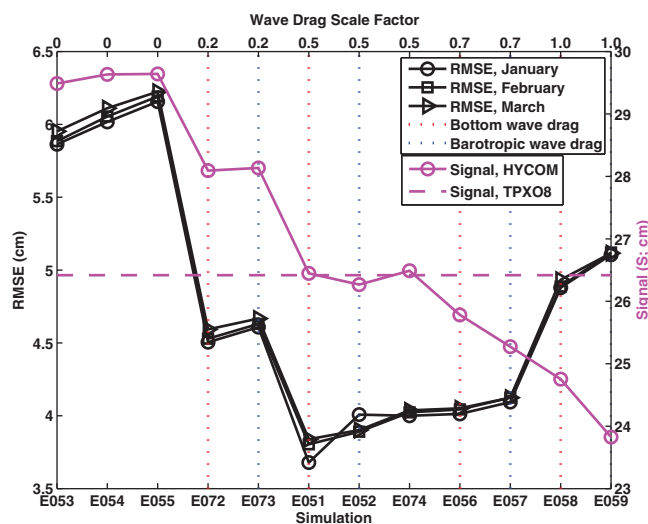
Figure 3. The root-mean-square error (RMSE; black curves) of HYCOM surface tidal elevations measured against TPXO8. The mean signal, S, in HYCOM and TPXO8 is depicted in the magenta curves (right axis). The scale factor of the wave drag for each simulation is shown on the top axis and the bottom and barotropic drag simulations are denoted by red and blue vertical dotted lines, respectively.

the barotropic-baroclinic system. As expected, the simulation with the smallest RMSE (E051) also has an S value that lies close to the TPXO8 value. The simulations without a wave drag (simulations E053, E054, and E055), even those with enhanced quadratic bottom friction along the shelves, have excessively large barotropic amplitudes.

A surprising outcome, at least to us, of the barotropic tidal analysis is how small the differences in the errors in Figure 3 are (<2.2 cm). As opposed to barotropic models [*Arbic et al.*, 2004; *Jayne and St. Laurent*, 2001; *Buijsman et al.*, 2015], and baroclinic models with only two layers [*Arbic et al.*, 2004], that show a large range in errors depending on whether wave drag is utilized or not, higher resolution baroclinic models with more vertical layers appear to show smaller ranges.

3.2. Baroclinic Tides
3.2.1. Steric Sea Surface Height Analyses

Before we compare the simulated global internal tides to along-track altimeter data, we first present the internal tides from the different scenarios. For this first look at internal tides, we use the steric SSH fields. The steric SSH refers to changes in sea level due to thermal expansions and salinity variations (i.e., the sea surface height component having to do with stratification effects). The steric SSH fields cover the entire globe and are direct model outputs without any contamination due to spatial band passing and/or interpolation of results to satellite tracks. The drawback of using steric SSH fields is the unavailability of observational data for comparison.

The amplitude of the M_2 internal tide signature in the steric sea surface height, recovered from a tidal harmonic analysis of 3 months of the model steric fields, is displayed in Figure 4. The beam-like structures of the tides radiating away from their generation sources [e.g., *Simmons et al.*, 2004] are readily apparent. The beams are generated in hot spot locations, which are depicted in Figure 4 by the rectangular regions taken from *Shriver et al.* [2012]. For each simulation, we compute the area-averaged root-mean-square amplitude (RMSA) over the globe, in each of the five subregions, and outside the subregions (see Table 2). This latter calculation provides a crude indication of how far the internal tides propagate away from their source regions.

The simulations without a wave drag (e.g., E053, E054, and E055; Figures 4e and 4f) generate highly energetic internal tides as seen in the global RMSA values (Table 2; column 1); in addition, the internal tides propagate far from their sources (Table 2; last column). This is also true of each of the subregions (Table 2) and can clearly be noticed in Figure 4. When the wave drag is applied to only the barotropic component of the flow (e.g., Figures 4b and 4d), the resulting internal tides also have large average amplitudes (and travel greater distances) compared to the simulations with the bottom wave drag (e.g., Figures 4a and 4c) although their amplitudes are not as large as those in simulations without a wave drag. By comparing the twin simulations of bottom (E072, E051, E056, and E058) and barotropic (E073, E052, E057, and E059) wave drag scenarios in Table 2, we find that the average amplitudes are consistently higher in the barotropic wave drag cases over the globe and for each subregion. In addition, the waves travel farther in the barotropic wave drag cases relative to the bottom drag cases. We note that simulation E073, which has the smallest scale factor (0.2) of the barotropic wave drag cases, gives values comparable to the simulations without a wave drag, suggesting that the scale factor 0.2 is too small to differentiate it from the no drag scenarios.
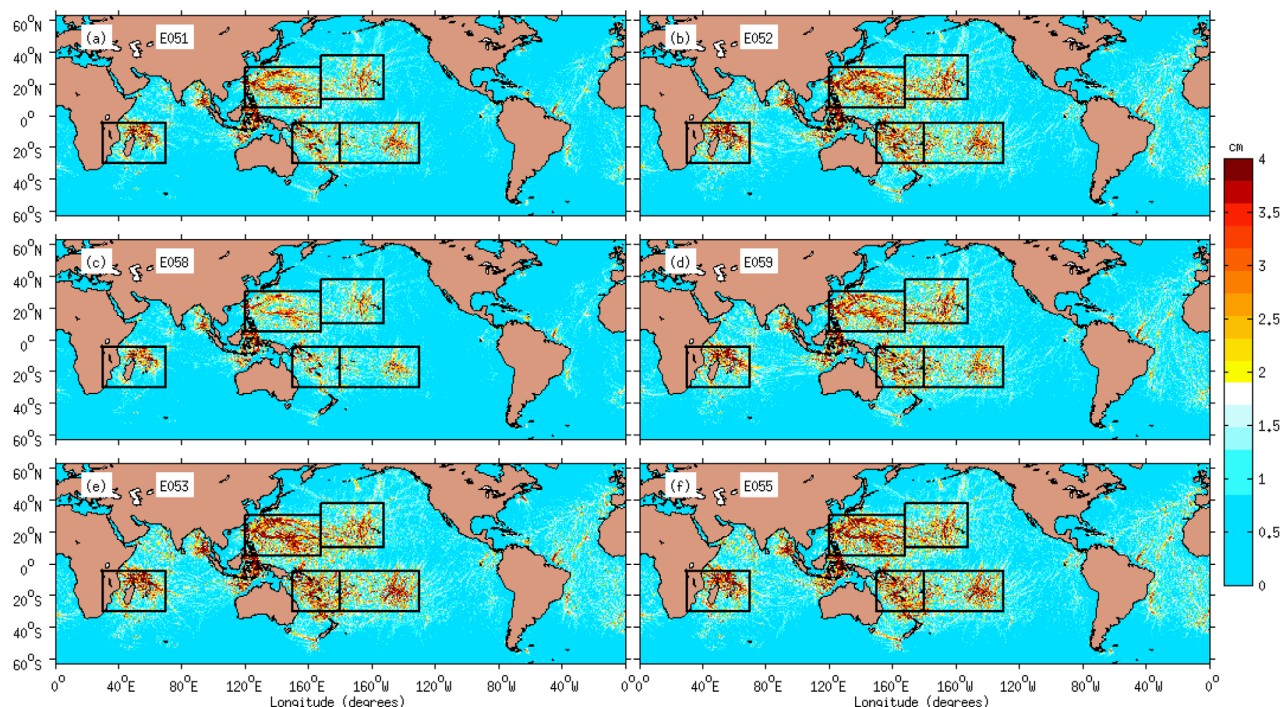
Figure 4. Amplitude of the M_2 surface elevations from the steric component, dominated by the internal tides, of the sea surface height in HYCOM simulations (a) E051; with wave drag (scale factor = 0.5) applied to the bottom flow, (b) E052; with wave drag (scale factor = 0.5) applied to only the barotropic flow, (c) E058; with wave drag (scale factor = 1.0) applied to the bottom flow, (d) E059; with wave drag (scale factor = 1.0) applied to only the barotropic flow, (e) E053; without wave drag, (f) E055; without wave drag but with quadratic bottom friction increased by about 100 times along the continental shelves. The amplitudes are computed from 3 months of SSH output.

3.2.2. Comparison to Along-Track Altimeter Data

Figure 5 displays maps of the SSH manifestation of the internal tides in HYCOM and in along-track altimeter data. The HYCOM results shown in Figure 5 all utilize 3 months of model output. Qualitatively, we find that the default configuration with a scale factor of 1.0 (Figure 5c; simulation E058) exhibits greater resemblance to the altimetric tides than the other scenarios with respect to both the scale of the tidal amplitudes and their spatial distribution. However, this should not be taken as indicating that simulation E058 yields the most accurate baroclinic tides because the results depend upon the length of time series used as we discuss shortly. A notable difference is that the internal tides in the Atlantic Ocean are somewhat weaker in the default HYCOM configuration (Figure 5c) than in the altimeter dataset. Reasons for such discrepancies have been expounded upon in *Shriver et al.* [2012] and range from errors in the barotropic tidal flows in HYCOM,

Table 2. Area-Averaged Root-Mean-Square Amplitudes (in cm) of the Steric Sea Surface Heights Over the Globe (Global) and in the Five Subregions Shown in Figure 4 Using 3 Month-Long SSH Output

Simulation	Global	Hawaii	East of Philippines	Tropical South Pacific	Tropical SW Pacific	Madagascar	Rest of World Ocean[a]
E053	1.153	1.967	2.751	2.130	2.707	2.215	0.847
E054	1.144	1.963	2.687	2.075	2.677	2.200	0.848
E055	1.142	1.977	2.731	2.058	2.660	2.181	0.843
E072	1.021	1.819	2.483	1.894	2.388	2.007	0.736
E073	1.154	2.024	2.710	2.091	2.738	2.224	0.851
E051	0.891	1.658	2.234	1.634	2.016	1.802	0.632
E052	1.067	1.923	2.533	1.942	2.524	2.122	0.775
E074	1.090	1.975	2.572	1.954	2.558	2.114	0.800
E056	0.828	1.548	2.055	1.508	1.869	1.719	0.588
E057	1.060	1.950	2.511	1.903	2.453	2.122	0.771
E058	0.760	1.465	1.893	1.374	1.649	1.614	0.536
E059	1.011	1.902	2.410	1.804	2.343	2.059	0.729

[a]The area-averaged amplitude for the rest of the world ocean outside the five hot spot regions.
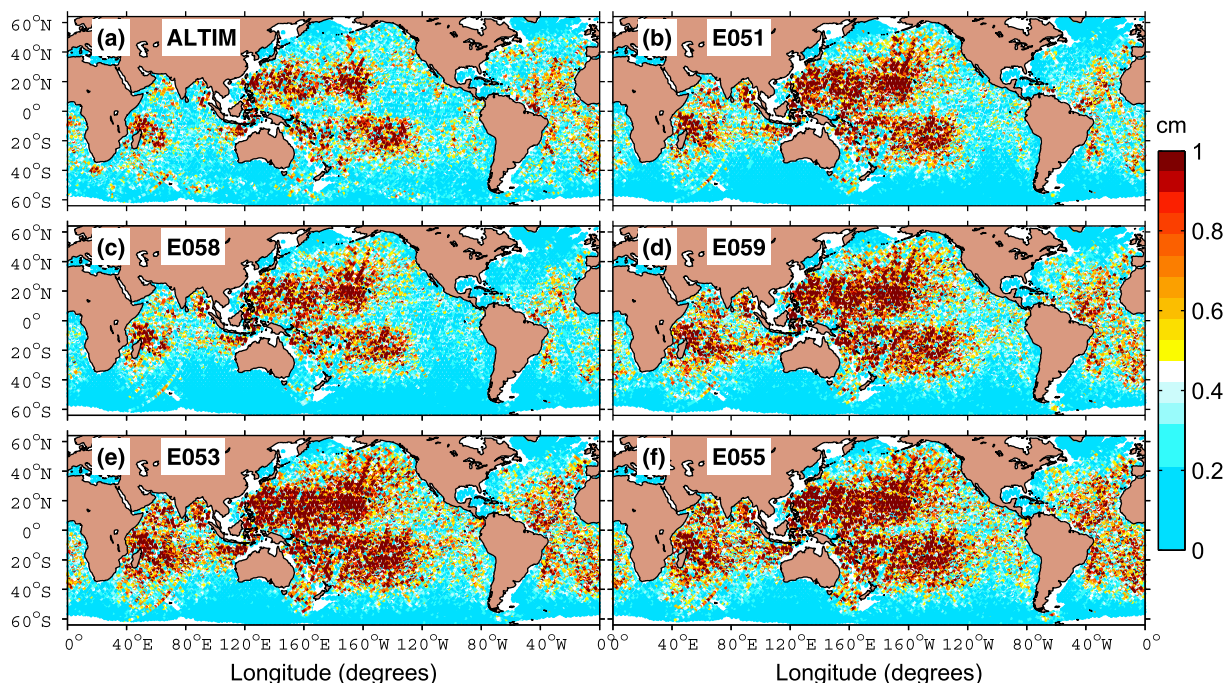
Figure 5. Amplitude (cm) of M_2 internal tide in (a) along-track altimeter-based analyses, and in HYCOM simulations (b) E051; with wave drag (scale factor = 0.5) applied to the bottom flow, (c) E058; with wave drag (scale factor = 1.0) applied to the bottom flow, (d) E059; with wave drag (scale factor = 1.0) applied to only the barotropic flow, (e) E053; without wave drag, (f) E055; without wave drag but with quadratic bottom friction increased by about 100 times along the continental shelves. The amplitudes of the HYCOM simulations are computed from 3 months of SSH output.

which generate internal tides, to mesoscale contamination in the altimeter data. In the absence of a wave drag on the bottom flow, we find the internal tides to be too energetic and to travel too far from their source regions (compare Figures 5e and 5f to Figure 5a).

Figure 6 affirms that the scenarios with wave drag acting on the bottom flow yield smaller discrepancies between HYCOM and the along-track altimeter data than do their counterparts with drag acting on only the barotropic flow. The RMSA in the barotropic wave drag simulations is reduced by 0.077 cm between no drag and drag scale factor 1.0, with an approximately linear dependence on the drag scale factor (Figure 7; blue curves), presumably due to the corresponding decrease in barotropic tide signal strength (Figure 3) leading to the generation of weaker internal tides. However, RMSA in the bottom wave drag simulations is reduced by the larger amount of 0.24 cm (Figure 7; red curves) between no drag and drag scale factor 1.0, indicating that the bottom wave drag effect on internal tides is due both to a reduction in the barotropic tides (which generate the baroclinic tides) and to a direct damping of the baroclinic tides after they are generated. The green curve in Figure 7b shows the difference in RMSA between
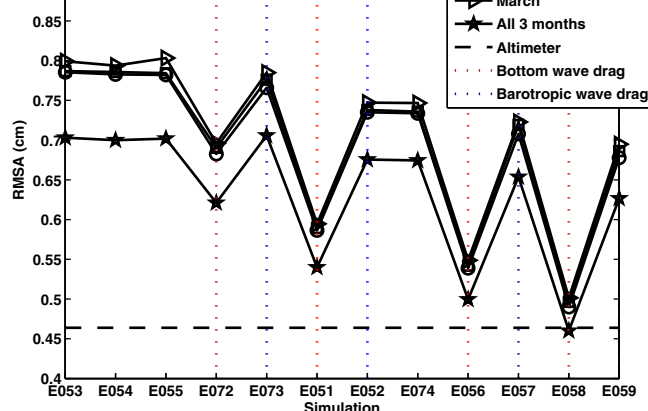
Figure 6. Globally averaged root-mean-square amplitude (RMSA), of HYCOM baroclinic tidal elevations from all simulations versus the along-track altimeter value. The scale factor of the wave drag for each simulation is shown on the top axis and the bottom and barotropic drag simulations are denoted by red and blue vertical dotted lines, respectively.
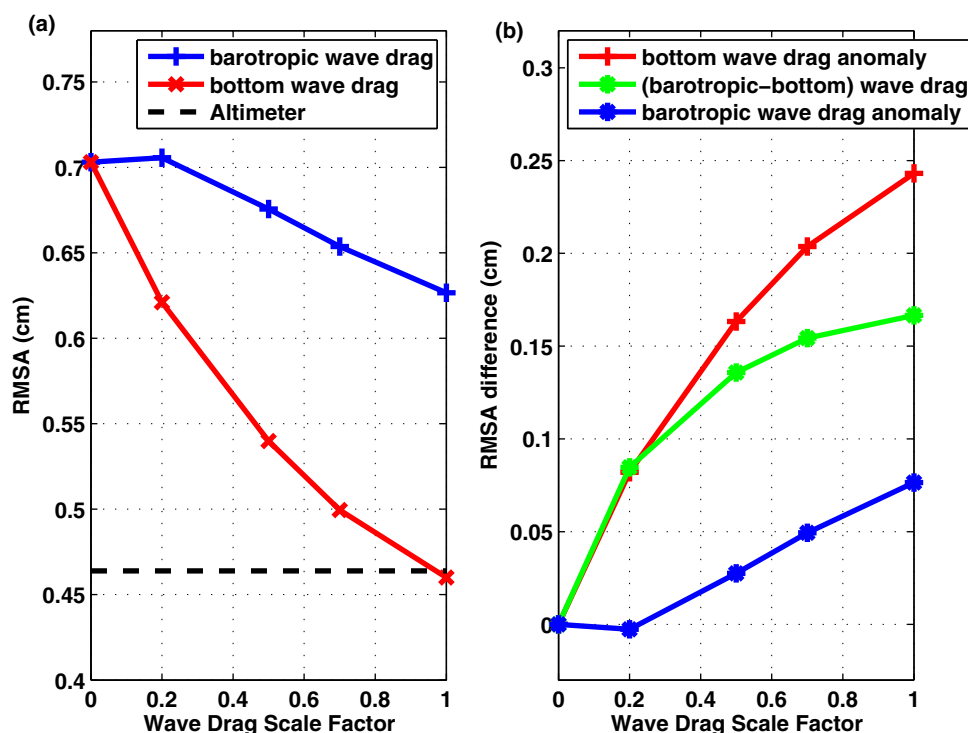
Figure 7. (a) Globally averaged root-mean-square amplitude (RMSA), of HYCOM baroclinic tidal elevations for the barotropic and bottom drag simulations shown in Figure 6 (from 3 months of analysis). (b) The difference in RMSA between the barotropic and bottom drag simulations in Figure 7a and their deviations from the no drag simulation.

the barotropic and bottom wave drag scenarios, increasing by 0.17 cm between no drag and drag scale factor 1.0. In scenarios without a wave drag (E053), even those with enhanced quadratic friction along the shelves (E054 and E055), the internal tides are too energetic and travel too far from the hot spot regions (see Figure 6 and Table 3). As can be seen in Table 3, the conclusions drawn above from the global analysis also apply to the five subregions. We analyzed a few 1/25° HYCOM simulations using 1 month of SSH output, and found that the internal tide results are consistent with results from our 1/12.5° simulations. More detailed results from the 1/25° simulations will be presented in the future; we do not further discuss them here for the sake of conciseness, simplicity, and computational expediency.

Table 3. Area-Averaged Amplitudes (in cm) of M_2 Internal Tides From HYCOM and Along-Track Altimetry (Altimeter) Over the Five Subregions Shown in Figure 4[a]

Simulation	Hawaii	East of Philippines	Tropical South Pacific	Tropical SW Pacific	Madagascar	Rest of World Ocean[b]
Altimeter	0.805	0.837	0.843	0.758	0.715	0.371
E053	1.294	1.530	1.270	1.234	1.223	0.516
E054	1.291	1.503	1.239	1.205	1.218	0.520
E055	1.304	1.547	1.225	1.203	1.210	0.519
E072	1.203	1.386	1.144	1.086	1.078	0.443
E073	1.329	1.507	1.248	1.252	1.230	0.520
E051	1.094	1.227	0.991	0.912	0.952	0.377
E052	1.304	1.470	1.179	1.188	1.187	0.493
E074	1.302	1.450	1.165	1.186	1.166	0.497
E056	1.029	1.104	0.924	0.847	0.904	0.349
E057	1.285	1.406	1.136	1.124	1.171	0.477
E058	0.971	1.028	0.847	0.748	0.830	0.319
E059	1.252	1.349	1.076	1.095	1.135	0.454

[a]The HYCOM results employ 3 month-long SSH output. All computations are for depths deeper than 1500 m.
[b]The area-averaged amplitude for the rest of the world ocean outside the five hot spot regions.
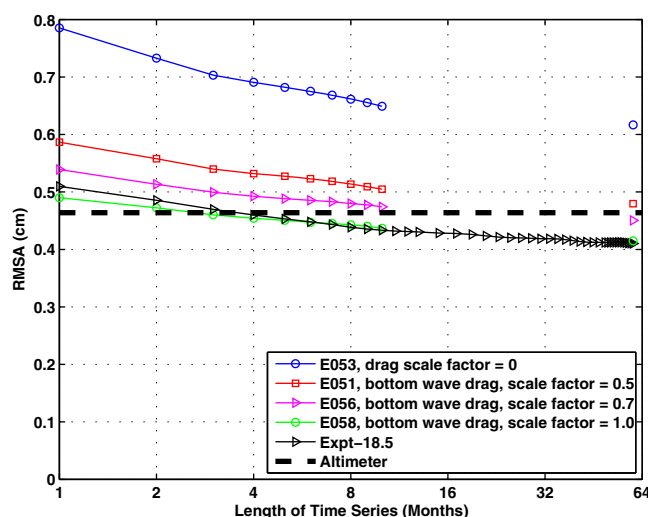
Figure 8. Globally averaged root-mean-square amplitude (RMSA), of HYCOM baroclinic tidal elevations and along-track altimeter value. The HYCOM results are dependent on drag strength (see legend) as well as on the length of the time series used. The x axis is a base 2 log scale. Expt-18.5 is an older HYCOM experiment from which several papers have been written [e.g., *Shriver et al.*, 2012] and from which 5 year-long SSH output was stored. The amplitudes shown at month 60 in our current simulations are rough estimates based on the change in Expt-18.5.

Figure 6 also shows that though there is little monthly variance in the globally averaged amplitudes, using 3 month-long time series for the analysis yields values that are reduced by about 9–15% from results computed from 1 month-long SSH output. This suggests that some of the discrepancies between the model and along-track altimeter data may be attributed to the length of model output used in the analysis. To further investigate the effect of the length of time series on the results, and to determine which simulation yields the most accurate internal tides, we run four simulations out longer, to obtain a total of 10 months of SSH hourly output. We run the simulations for only 10 months because we only have hourly NAVGEM forcing over this period. In this exercise, we considered the no drag simulation, E053, and three simulations with bottom wave drag: E051 (drag scale 0.5), E056 (drag scale 0.7), and E058 (drag scale 1.0). Because the M_2 internal tide amplitudes in the four simulations are still decreasing after 10 months of analysis (Figure 8), we also analyzed an older HYCOM simulation (Expt-18.5; Figure 8) from which 5 year-long SSH output was saved. We find that the internal tide amplitudes in Expt-18.5 converge to an asymptotic value after about 4 years, reducing from RMSA value of 0.43 cm at 10 months to an average value of 0.41 cm after 4 years, a reduction in amplitude of about 5%. To obtain rough estimates of RMSA from the four other simulations considered in Figure 8, we use the Expt-18.5 results as a correction to them, suggesting that the four simulations E053, E051, E056, and E058 will likely asymptote to 0.62, 0.48, 0.45, and 0.42 cm, respectively, after about 4 years. The estimated asymptotic values for these four simulations are shown at month 60 in Figure 8. This exercise suggests that the along-track altimeter value of 0.46 cm will lie between that of simulation E056 (bottom wave drag; scale factor 0.7) and E051 (bottom wave drag; scale factor 0.5) with E056 yielding a value slightly closer to the altimeter value than E051. Because the RMSA values of E056 and E051 are both very close to the altimeter value and because the corrections discussed above are based on results from an older simulation, it is still not clear which of the two simulations is superior to the other. However, both simulations are more accurate than the older simulation, Expt-18.5, and importantly for this paper, both are more accurate than the no-wave-drag simulation (E053). Figure 8 shows that both the record duration and the drag impact the coherent internal tide amplitudes. It is not clear that the impact of record duration is due to an estimation problem in the presence of background noise or to nonstationarity. The results on the impact of record duration shown in Figure 8 are consistent with those of *Zhou et al.* [2015], which indicate that the internal tide variance from an hourly sampled mooring record flattens out in about 3 years (their Figure 4; open circles), as well as with related results in *Nash et al.* [2012].

4. Summary and Conclusions

In order to roughly constrain the damping of low-mode internal tides, we have conducted numerical simulations with a high-resolution eddy-resolving global ocean circulation model (HYCOM) forced by the M_2 tidal constituent and atmospheric fields. Various damping scenarios with different strengths of parameterized internal wave drag or quadratic bottom friction are performed. We ran simulations in

which a parameterized wave drag scheme was either applied to the bottom flow (referred to as "bottom wave drag" or the "default configuration" here) or to the barotropic component of the flow (referred to as "barotropic wave drag"). We argue that parameterized wave drag represents the breaking of unresolved high modes by barotropic and low-mode baroclinic flows over open ocean rough topography. In another simulation (designated here as E053), the wave drag is completely turned off and the only drag on the flow is quadratic bottom friction. Finally, to test whether the propagating low-mode internal tides dissipate mostly on the continental shelves, we turn off the wave drag (or apply it only to the barotropic flow) and at the same time substantially increase the quadratic bottom friction along the shelves. We consider two cases (simulation E054 and E055) in which the bottom friction in shelf regions is increased by about 25 and 100 times, respectively, above the canonical deep ocean value of 0.0025. To test the plausibility of the various damping scenarios, the resulting barotropic tides in each simulation are compared to the data-assimilative TPXO8-atlas solution. The baroclinic tides are compared to about 17 years of along-track altimeter data.

The barotropic tides in our simulations with bottom wave drag (especially simulation E051) compare reasonably well with TPXO8. Scenarios without a wave drag in the open ocean result in barotropic tides that are more energetic in HYCOM than in TPXO8. For the barotropic tides, we find that the differences in the root-mean-square error (RMSE) between the simulations are relatively small (about 2 cm).

The discrepancies between the baroclinic tides and the altimeter data vary more significantly in the tested scenarios. In the runs analyzed for this paper, the simulations with wave drag acting on the bottom flow result in the most accurate baroclinic tides. In simulations in which a wave drag is turned off entirely, or in which it acts on only the barotropic flow, the baroclinic tides are overly energetic and propagate too far from the hot spot regions, even in the simulations (E054 and E055) in which quadratic bottom friction is greatly increased in shelf regions. All of this suggests that, although some internal tidal damping takes place along the shelves [*Nash et al.*, 2004; *Martini et al.*, 2011; *Kelly et al.*, 2013; *Waterhouse et al.*, 2014], substantial low-mode damping likely occurs in the deep ocean. *Waterhouse et al.* [2014] estimate that about 30% of the internal tide energy reaches into the shelves from the open ocean. Their 30% result is not inconsistent with our conclusion that a substantial damping also takes place in the open ocean. Analysis of an older HYCOM simulation (M. C. Buijsman et al., submitted manuscript, 2015) indicates that bottom wave drag damps about 40% of internal tide energy, and that inferred residual numerical damping may dissipate about 30–40% of the internal tide energy. More analysis, including of the residual damping, needs to be performed before a final accounting can be made of the partitioning of internal tide damping between various mechanisms.

We have found that the duration of model output, as well as the damping strength, affects the comparison of modeled internal tides to satellite altimetry. Figure 8 demonstrates that the globally averaged internal tide amplitudes in our simulations require about 3–4 years to converge. The long time required for convergence is consistent with results in *Nash et al.* [2012] and *Zhou et al.* [2015], who both analyzed tide records at individual locations. It is not clear whether this is due to an estimation problem in the presence of background noise or to nonstationarity, and additional studies are required to determine the underlying cause. We note that an increasing number of internal tide studies conclude that internal tide incoherence is a substantial effect. *Zaron* [2015], for example, finds that about one-third of the global semidiurnal internal tide sea surface height variance is incoherent. Using 5 year-long SSH output from an older HYCOM experiment, we estimate asymptotic values of the M_2 amplitudes for four of our simulations (E053, E051, E056, and E058; Figure 8), and find that simulations E051 (bottom wave drag with scale factor 0.5) and E056 (bottom wave drag with scale factor 0.7) yield the most accurate baroclinic tides.

We reiterate that our simulations represent various limiting cases of the aforementioned damping mechanisms. Other plausible scenarios for damping low-mode internal tides, such as upper-ocean wave-wave interactions, have not been tested in this study and will instead be investigated separately. It remains to be seen whether upper-ocean wave-wave interactions represent an open ocean damping mechanism that is equally plausible as bottom wave drag. In the actual ocean, of course, more than one mechanism is likely to be important. We leave it to future work to examine model runs having more than one open ocean damping mechanism acting simultaneously, an endeavor considered to be too complicated for the present paper.

In future work, we will examine in more detail the impacts of record duration and model resolution. We will also examine the energy budgets in simulations with different drag strengths.

References

Alford, M. H., and Z. Zhao (2007), Global patterns of low-mode internal-wave propagation. Part I: Energy and Energy flux, *J. Phys. Oceanogr.*, *37*, 1829–1848.

Arbic, B. K., S. T. Garner, R. W. Hallberg, and H. L. Simmons (2004), The accuracy of surface elevations in forward global barotropic and baroclinic tide models, *Deep Sea Res., Part II*, *51*, 3069–3101.

Arbic, B. K., A. J. Wallcraft, and E. J. Metzger (2010), Concurrent simulation of the eddying general circulation and tides in a global ocean model, *Ocean Modell.*, *32*, 175–187.

Arbic, B. K., J. G. Richman, J. F. Shriver, P. G. Timko, E. J. Metzger, and A. J. Wallcraft (2012), Global modeling of internal tides within an eddying ocean general circulation model, *Oceanography*, *25*(2), 20–29.

Bleck, R. (2002), An oceanic general circulation model framed in hybrid isopycnic-Cartesian coordinates, *Ocean Modell.*, *37*, 55–88.

Buijsman, M. C., S. Legg, and J. Klymak (2012), Double ridge internal tide interference and its effect on dissipation in luzon strait, *J. Phys. Oceanogr.*, *42*, 1337–1356.

Buijsman, M. C., B. K. Arbic, J. A. M. Green, R. W. Helber, J. G. Richman, J. F. Shriver, P. G. Timko, and A. J. Wallcraft (2015), Optimizing internal wave drag in a forward barotropic model with semidiurnal tides, *Ocean Modell.*, *85*, 42–55.

Carter, G. S., O. B. Fringer, and E. D. Zaron (2012), Regional models of internal tides, *Oceanography*, *25*(2), 56–65.

Chassignet, E. P., L. T. Smith, G. R. Halliwell, and R. Bleck (2003), North Atlantic simulations with the Hybrid Coordinate Ocean Model (HYCOM): Impact of the vertical coordinate choice, reference pressure, and thermobaricity, *J. Phys. Oceanogr.*, *33*, 2504–2526.

Cummins, P. E., and L. Y. Oey (1997), Simulation of barotropic and baroclinic tides off Northern British Columbia, *J. Phys. Oceanogr.*, *27*, 762–781.

Dunphy, M., and K. G. Lamb (2014), Focusing and vertical mode scattering of the first mode internal tide by mesoscale eddy interaction, *J. Geophys. Res.*, *119*, 523–536, doi:10.1002/2013JC009293.

Dushaw, B. D., P. F. Worcester, B. D. Cornuelle, B. M. Howe, and D. S. Luther (1995), Baroclinic and barotropic tides in the central North-Pacific Ocean determined from long-range reciprocal acoustic transmissions, *J. Phys. Oceanogr.*, *25*, 631–647.

Egbert, G. G., and S. Y. Erofeeva (2002), Efficient inverse modeling of barotropic ocean tides, *J. Atmos. Oceanic Technol.*, *19*, 183–204.

Egbert, G. G., and R. D. Ray (2000), Significant dissipation of tidal energy in the deep ocean inferred from satellite altimeter data, *Nature*, *405*, 775–778.

Egbert, G. G., and R. D. Ray (2001), Estimates of M_2 tidal energy dissipation from TOPEX/POSEIDON altimeter data, *J. Geophys. Res.*, *106*, 22,475–22,502.

Egbert, G. D., R. D. Ray, and B. G. Bills (2004), Numerical modeling of the global semidiurnal tide in the present day and in the last glacial maximum, *J. Geophys. Res.*, *109*, C03003, doi:10.1029/2003JC001973.

Garner, S. T. (2005), A topographic drag closure built on an analytical base flux, *J. Atmos. Sci.*, *62*, 2302–2315.

Green, J. A. M., and J. Nycander (2013), A comparison of tidal conversion parameterizations for tidal models, *J. Phys. Oceanogr.*, *43*, 104–119.

Halliwell, G. R. (2004), Evaluation of vertical coordinate and vertical mixing algorithms in the HYbrid-Coordinate Ocean Model (HYCOM), *Ocean Modell.*, *7*, 285–322.

Hecht, M. W., and H. Hasumi (Eds.) (2008), *Ocean Modeling in an Eddying Regime, Geophys. Monogr. 117*, 409 pp., AGU, Washington, D. C., doi:10.1029/GM177.

Hendershott, M. C. (1972), The effects of solid earth deformation on global ocean tides, *Geophys. J. R. Astron. Soc.*, *29*, 389–402.

Hogan, T. F., et al. (2014), The Navy Global Environmental Model, *Oceanography*, *27*(3), 116–125.

Hunke, E. C., and W. Lipscomb (2008), CICE: The Los Alamos Sea Ice Model: Documentation and Software User's Manual, Version 4.0, *Tech. Rep. LA-CC-06–012*, Los Alamos Natl. Lab., Los Alamos, N. M.

Jayne, S. R., and L. C. St. Laurent (2001), Parameterizing tidal dissipation over rough topography, *Geophys. Res. Lett.*, *28*, 811–814.

Johnston, T. M. S., and M. A. Merrifield (2003), Internal tide scattering at seamounts, ridges and islands, *J. Geophys. Res.*, *108*(C6), 3180, doi:10.1029/2002JC001528.

Kelly, S. M., N. L. Jones, J. D. Nash, and A. F. Waterhouse (2013), The geography of semidiurnal mode-1 internal-tide energy loss, *Geophys. Res. Lett.*, *40*, 4689–4693, doi:10.1002/grl.50872.

Kerry, C., B. Powell, and G. Carter (2014), The impact of subtidal circulation on internal-tide-induced mixing in the Philippine sea, *J. Phys. Oceanogr.*, *44*, 3209–3224.

Klymak, J. M., J. N. Moum, J. D. Nash, E. Kunze, J. B. Girton, G. S. Carter, C. M. Lee, T. B. Sanford, and M. C. Gregg (2006), An estimate of tidal energy lost to turbulence at the Hawaiian Ridge, *J. Phys. Oceanogr.*, *36*, 1148–1164.

Klymak, J. M., R. Pinkel, and L. Rainville (2008), Direct breaking of the internal tides near topography: Kaena Ridge, Hawaii, *J. Phys. Oceanogr.*, *38*, 380–399.

Kunze, E., and S. G. Llewellyn Smith (2004), The role of small-scale topography in turbulent mixing of the global ocean, *Oceanography*, *17*, 55–64.

Legg, S., and J. Klymak (2008), Internal hydraulic jumps and overturning generated by tidal flow over a tall steep ridge, *J. Phys. Oceanogr.*, *38*, 1949–1964.

MacKinnon, J., and K. Winters (2005), Subtropical catastrophe: Significant loss of low-mode tidal energy at 28.9°, *Geophys. Res. Lett.*, *32*, L15605, doi:10.1029/2005GL023376.

Martini, K. I., M. H. Alford, E. Kunze, S. M. Kelly, and J. D. Nash (2011), Observations of internal tides on the Oregon continental slope, *J. Phys. Oceanogr.*, *41*, 1772–1794.

Mathur, M., G. S. Carter, and T. Peacock (2014), Topographic scattering of the low-mode internal tide in the deep ocean, *J. Geophys. Res. Oceans*, *119*, 2165–2182, doi:10.1002/2013JC009152.

McComas, C. H., and F. P. Bretherton (1977), Resonant interactions of oceanic internal waves, *J. Phys. Oceanogr.*, *82*(9), 1397–1412.

Mitchum, G. T., and S. M. Chiswell (2000), Coherence of internal tide modulations along the Hawaiian ridge, *J. Geophys. Res.*, *105*, 28,653–28,661.

Müller, M., J. Y. Cherniawsky, M. G. G. Foreman, and J. S. Storch von (2012), Global M_2 internal tide and its seasonal variability from high resolution ocean circulation and tide modeling, *Geophys. Res. Lett.*, *39*, L19607, doi:10.1029/2012GL053320.

Müller, M., B. K. Arbic, J. G. Richman, J. F. Shriver, E. L. Kunze, R. B. Scott, A. J. Wallcraft, and L. Zamudio (2015), Toward an internal gravity wave spectrum in global ocean models, *Geophys. Res. Lett.*, *42*, 3474–3481, doi:10.1002/2015GL063365.

Müller, P., G. Holloway, F. Henyey, and N. Pomphrey (1986), Nonlinear interactions among internal gravity waves, *Rev. Geophys.*, *24*(3), 493–536.

Munk, W. (1966), Abyssal recipes, *Deep Sea Res. Oceanogr. Abstr.*, *13*, 707–730.

Munk, W., and C. Wunsch (1998), Abyssal recipes ii: Energetics of tidal and wind mixing, *Deep Sea Res., Part I*, *45*, 1977–2010.

Nash, J. D., E. Kunze, J. M. Toole, and R. W. Schmitt (2004), Internal tide reflection and turbulent mixing on the continental slope, *J. Phys. Oceanogr.*, *34*, 1117–1134.

Nash, J. D., E. L. Shroyer, S. M. Kelly, M. E. Inall, T. F. Duda, M. D. Levine, N. L. Jones, and R. C. Musgrave (2012), Are any coastal internal tides predictable?, *Oceanography*, *25*(2), 80–95, doi:10.5670/oceanog.2012.44.

Niwa, Y., and T. Hibiya (2001), Numerical study of the spatial distribution of the M_2 internal tide in the Pacific Ocean, *J. Geophys. Res.*, *106*, 22,441–22,449.

Niwa, Y., and T. Hibiya (2011), Estimation of baroclinic tide energy available for deep ocean mixing based on three-dimensional global numerical simulations, *J. Oceanogr.*, *67*, 493–502.

Oey, L. Y. (2006), An OGCM with movable land-sea boundaries, *Ocean Modell.*, *13*, 176–195.

Rainville, L., and R. Pinkel (2006), Baroclinic energy flux at the Hawaiian Ridge: Observations from the R/P FLIP, *J. Phys. Oceanogr.*, *36*, 1104–1122.

Ray, R. D., and D. A. Byrne (2010), Bottom pressure tides along a line in the southeast Atlantic Ocean and comparisons with satellite altimetry, *Ocean Dyn.*, *60*, 1167–1176.

Ray, R. D., and G. T. Mitchum (1996), Surface manifestation of internal tides generated near Hawaii, *Geophys. Res. Lett.*, *23*, 2101–2104.

Ray, R. D., and G. T. Mitchum (1997), Surface manifestation of internal tides in the deep ocean: Observations from altimetry and tide gauges, *Prog. Oceanogr.*, *40*, 135–162.

Richman, J. G., B. K. Arbic, J. F. Shriver, E. J. Metzger, and A. J. Wallcraft (2012), Inferring dynamics from the wavenumber spectra of an eddying global ocean model with embedded tides, *J. Geophys. Res.*, *117*, C12012, doi:10.1029/2012JC008364.

Rosmond, T. E., J. Teixeira, M. Peng, T. F. Hogan, and R. Pauley (2002), Navy Operational Global Atmospheric Prediction System (NOGAPS): Forcing for ocean models, *Oceanography*, *15*, 99–108.

Schlichting, H. (1968), *Boundary Layer Theory*, McGraw-Hill, N. Y.

Shriver, J. F., B. K. Arbic, J. G. Richman, R. D. Ray, E. J. Metzger, A. J. Wallcraft, and P. G. Timko (2012), An evaluation of the barotropic and internal tides in a high resolution global ocean circulation model, *J. Geophys. Res.*, *117*, C10024, doi:10.1029/2012JC008170.

Shriver, J. F., J. G. Richman, and B. K. Arbic (2014), How stationary are the internal tides in a high resolution global ocean circulation model?, *J. Geophys. Res.*, *119*, 2769–2787, doi:10.1002/2013JC009423.

Simmons, H. L. (2008), Spectral modification and geographic redistribution of the semi-diurnal internal tide, *Ocean Modell.*, *21*, 126–138.

Simmons, H. L., R. W. Hallberg, and B. K. Arbic (2004), Internal wave generation in a global baroclinic tide model, *Deep Sea Res., Part II*, *51*, 3043–3068.

St. Laurent, L., and C. Garrett (2002), The role of internal tides in mixing the deep ocean, *J. Phys. Oceanogr.*, *32*, 2882–2899.

Staquet, C., and J. Sommeria (2002), Internal gravity waves: From instability to turbulence, *Annu. Rev. Fluid Mech.*, *34*, 559–593.

Sun, O. M., and R. Pinkel (2012), Energy transfer from high-shear, low-frequency internal waves to high-frequency waves near Kaena Ridge, Hawai'i, *J. Phys. Oceanogr.*, *42*, 1524–1547, doi:10.1175/JPO-D-11-0117.1.

Sun, O. M., and R. Pinkel (2013), Subharmonic energy transfer from the semidiurnal internal tide to near-diurnal motions over Kaena Ridge, Hawai'i, *J. Phys. Oceanogr.*, *43*, 766–789, doi:10.1175/JPO-D-12-0141.1.

Thoppil, P. G., J. G. Richman, and P. J. Hogan (2011), Energetics of a global ocean circulation model compared to observations, *Geophys. Res. Lett.*, *38*, L15607, doi:10.1029/2011GL048347.

Timko, P. G., B. K. Arbic, J. G. Richman, R. B. Scott, E. J. Metzger, and A. J. Wallcraft (2012), Skill tests of three-dimensional tidal currents in a global ocean model: A look at the North Atlantic, *J. Geophys. Res.*, *117*, C08014, doi:10.1029/2011JC007617.

Timko, P. G., B. K. Arbic, J. G. Richman, R. B. Scott, E. J. Metzger, and A. J. Wallcraft (2013), Skill testing a three-dimensional global tide model to historical current meter records, *J. Geophys. Res.*, *118*, 6914–6933, doi:10.1002/2013JC009071.

Waterhouse, A. J., et al. (2014), Global patterns of diapycnal mixing from measurements of the turbulent dissipation rate, *J. Phys. Oceanogr.*, *44*, 1854–1872.

Wunsch, C., and R. Ferrari (2004), Vertical mixing, energy and the general circulation of the ocean, *Annu. Rev. Fluid Mech.*, *36*, 281–314.

Zaron, E. D. (2015), Non-stationary internal tides observed using dual-satellite altimetry, *J. Phys. Oceanogr*, doi:10.1175/JPO-D-15-0020.1, in press.

Zhao, Z., M. H. Alford, J. A. MacKinnon, and R. Pinkel (2010), Long-range propagation of the semi-diurnal internal tide from the Hawaiian ridge, *J. Phys. Oceanogr.*, *40*, 713–736.

Zhou, X. H., D. P. Wang, and D. Chen (2015), Validating satellite altimeter measurements of internal tides with long-term TAO/TRITON buoy observations at 2°S–156°E, *Geophys. Res. Lett.*, *42*, 4040–4046, doi:10.1002/2015GL063669.